






# Solution-Processed Epitaxial Growth of Arbitrary Surface Nanopatterns on Hybrid Perovskite Monocrystalline Thin Films

Jinshuai Zhang<sup>†</sup>,  Qin Guo<sup>†</sup>, Xuan Li<sup>†</sup>, Chao Li<sup>‡</sup>, Kan Wu<sup>‡</sup>, Isaac Abrahams<sup>§</sup>,  Haixue Yan<sup>†</sup>,   
Martin M. Knight<sup>†</sup>,  Colin J. Humphreys<sup>†</sup>  and Lei Su<sup>\*†</sup> 

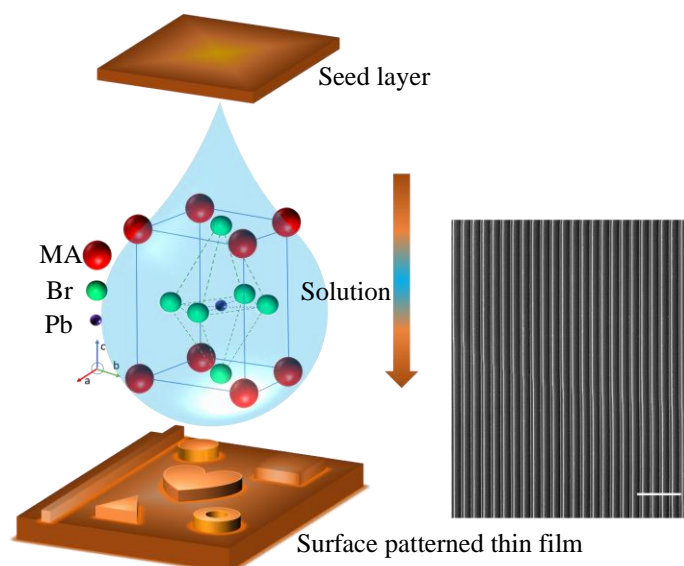
<sup>†</sup>School of Engineering and Materials Science, Queen Mary University of London, Mile End Road, London E1 4NS, United Kingdom

<sup>‡</sup>State Key Laboratory of Advanced Optical Communication Systems and Networks, Department of Electronic Engineering, Shanghai Jiao Tong University, Shanghai 200240, China

<sup>§</sup> School of Biological and Chemical Sciences, Queen Mary University of London, Mile End Road, London E1 4NS, United Kingdom

Email: l.su@qmul.ac.uk

**ABSTRACT:** Semiconductor surface patterning at the nanometre scale is crucial for high-performance optical, electronic and photovoltaic devices. To date, surface nanostructures on organic-inorganic single-crystal perovskites have been achieved mainly through destructive methods such as electron-beam lithography and focused ion beam milling. Here, we present a solution-based epitaxial-growth method for creating nanopatterns on the surface of perovskite monocrystalline thin films. We show that high-quality monocrystalline arbitrary nanopatterns can form in solution with a low-cost simple setup. We also demonstrate controllable photoluminescence from nanopatterned perovskite surfaces by adjusting the nanopattern parameters. A seven-fold enhancement in photoluminescence intensity and a three-time reduction of the surface radiative recombination lifetime are observed at room temperature for nanopatterned MAPbBr<sub>3</sub> monocrystalline thin films. Our findings are promising for the cost-effective fabrication of monocrystalline perovskite on-chip electronic and photonic circuits down to the nanometre scale with finely tuneable optoelectronic properties.



**KEYWORDS:** *perovskite, epitaxial growth, nanopatterns, single crystal, photoluminance, Mie resonance*

Hybrid organometal halide perovskites  $\text{MAPbX}_3$  (where  $\text{MA} = \text{CH}_3\text{NH}_3^+$ ,  $\text{X} = \text{I}^-$ ,  $\text{Br}^-$  or  $\text{Cl}^-$ ) have emerged as a promising candidate for high-performance photovoltaic and optoelectronic devices, exhibiting a range of excellent properties including strong light absorption, direct bandgaps, long carrier lifetime, high balanced hole and electron mobilities,<sup>1, 2</sup> and long electron-hole diffusion lengths.<sup>3</sup> Hybrid perovskites have been demonstrated in solar cells,<sup>4</sup> photodetectors,<sup>5</sup> lasers<sup>6</sup> and light emitting diodes (LEDs).<sup>7</sup>

Patterning semiconductor surfaces is important for various applications in nanoelectronics and nanophotonics.<sup>8-13</sup> Patterning using moulds made on polydimethylsiloxane (PDMS) and silicon *etc.* has been proposed to form periodic structures on the surface of perovskites, with the aims of improving the power conversion efficiency for solar cells<sup>14</sup> and enhancing photodetector performances.<sup>15</sup> as well as applications in photonic crystals<sup>16</sup> and distributed feedback lasers.<sup>17</sup> Polycrystalline perovskite thin-film nanopatterns are relatively easy to make, usually through spin coating and solution nanoimprinting or patterning.<sup>15, 16, 18</sup> However, there is no suitable method for developing high-quality single-crystal arbitrary surface nanopatterns on monocrystalline perovskite thin films, due to the following main limiting factors. Firstly, conventional one-step nanoimprinting and patterning methods are limited to making polycrystalline perovskite nanopatterns,<sup>14-17</sup> nanowires<sup>19-22</sup> and microplates.<sup>23, 24</sup> Secondly, it is difficult to apply widely-used lithography-based methods, as a result of the sensitivity of metalorganic perovskites to high temperature<sup>25</sup> and polar solvents<sup>26</sup> such as water, acetone and methanol. For

example, direct patterning of perovskites through electron-beam lithography (EBL) usually leads to unexpected phase transformations or defects due to the local heating induced by high-energy electrons.<sup>27</sup> Focused ion beam (FIB) milling<sup>28, 29</sup> is likely to degrade the optical properties of perovskites. Hence, methods for making high-quality single-crystal perovskite surface patterns are needed.

Interestingly, in our MAPbBr<sub>3</sub> single crystal growing experiment using the inverse temperature method,<sup>30-32</sup> the surface morphology at the bottom of the beaker was transferred to the contact surface of the single crystal (Supporting Information S1 and S2). A space-confined method<sup>21, 33-35</sup> was also recently proposed to synthesise single-crystalline perovskite thin films, where ultra-smooth single-crystal perovskite thin films were obtained with a controllable thickness. Furthermore, Gao *et al.*<sup>36</sup> reported the space-confined one-step growth of single-crystal pillar arrays. However, such one-step space-confined methods are only limited to the growth of nanostructures of certain shapes, but not for arbitrary nanopatterns. Alternatively, one may propose the use of a nanostructured template for the epitaxial growth of arbitrary single-crystalline perovskite thin-film surface nanopatterns using the space-confined method. This, however, is likely to fail, because the interface between the nanostructured template and the solution functions as a crystallisation-friendly site and this leads undesirably to many seed-crystal formations in one small area. These multiple seed crystals eventually grow into a polycrystalline thin film (Supporting Information S3).

In this paper, combining the surface morphology transferrable property and the space-confined method, we present a cost-effective, simple, non-destructive and solution-processed epitaxial growth method to form arbitrary single-crystal nanopatterns on monocrystalline thin films. We employ a two-step approach, first to use the space-confined method to grow a monocrystalline thin film, and then transfer patterns to the thin film surface in the second step. Figure 1 summarises the procedure. In the first step, the perovskite solution drops are made on the substrate and fills in the gap between the two substrates (such as Si, SiO<sub>2</sub>/Si, ITO, FTO *etc.*) as a result of capillary action. The substrates are then heated to reach an oversaturated temperature point, at which the perovskite single crystals start to nucleate and grow. The gap distance between the two substrates, controlled by spacers, determines the thickness of the perovskite monocrystalline thin film. In the second step, the prepared monocrystalline thin film is used as a seed layer. Thicker spacers are used to allow additional growth, and the upper substrate is replaced by a nanopatterned PDMS template. The same concentration of perovskite solution as that used in Step 1 is used here,

while the solution temperature is maintained at a lower point to avoid the formation of new seed crystals. As shown in the final stage of the experiment, the growth space is confined by the nanopatterned PDMS template and the substrate, and the epitaxial growth of single-crystal perovskite nanopatterns is subsequently achieved.

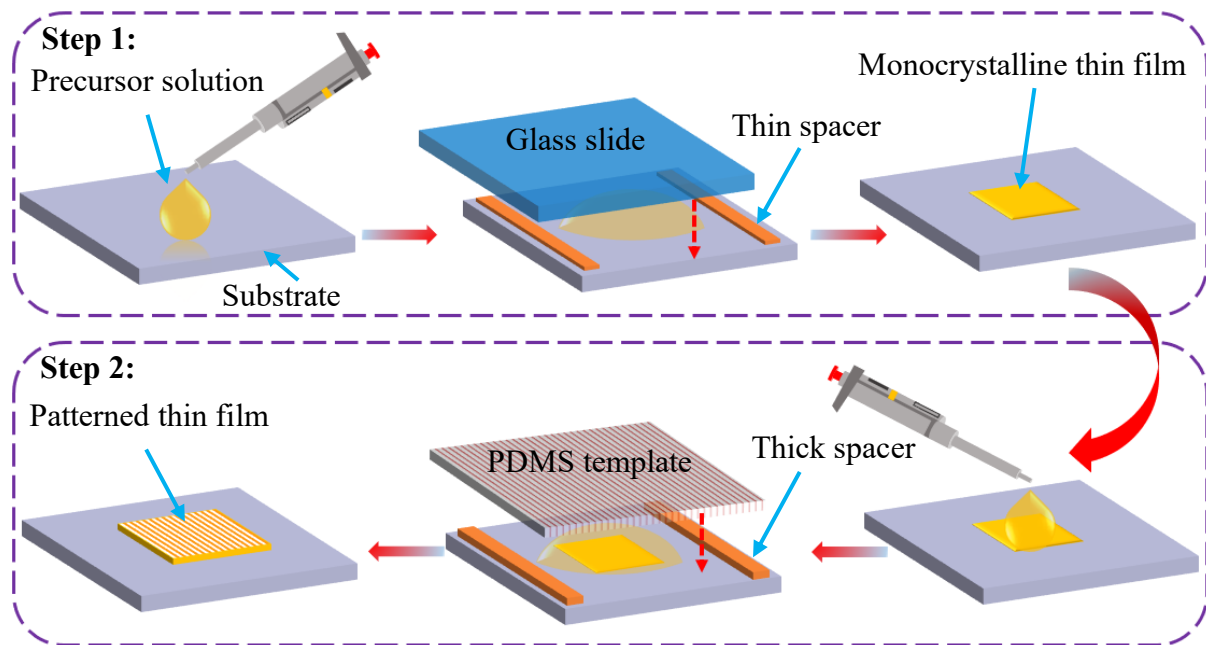
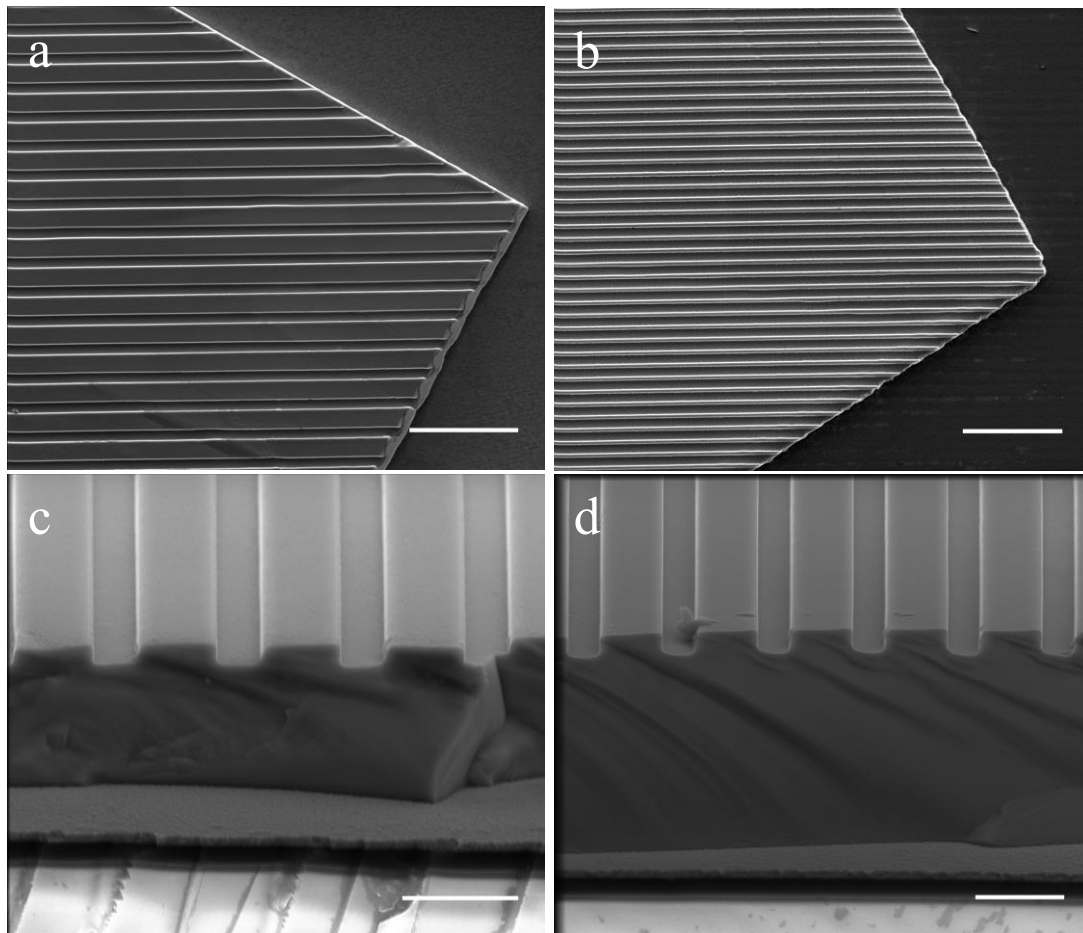


**Figure 1.** Schematic illustration of the two-step patterning approach for the fabrication of surface nano-structures on monocrystalline perovskites. Step 1:  $\text{MAPbBr}_3$  solution drops are made on the substrate and fills the gap between two substrates. Afterwards, monocrystalline thin film forms at the high temperature heating process. Step 2: The same  $\text{MAPbBr}_3$  solution drops are made on the substrate on which the monocrystalline thin film forms in the Step 1. Then thicker spacers are used together with a patterned PDMS template as the top substrate. Finally, a perovskite monocrystalline thin film with the same surface nanopatterns as the PDMS template is formed through epitaxial growth.

## RESULTS

Scanning electron microscopy (SEM) was conducted on patterned monocrystalline thin films with surface periodic gratings fabricated using the method described above. These nano-grating structures were first transferred to PDMS templates from Si masks with different patterns (see EXPERIMENTAL for details). Patterns 1-4 had different stripe and trench widths as follows: Pattern 1 (stripe 600 nm and trench 1500 nm), Pattern 2 (stripe 740 nm and trench 1500 nm), Pattern 3 (strip 1500 nm and trench 740 nm) and Pattern 4 (strip 3000 nm and trench 1500 nm). The SEM images in Supporting

Information S4a-d revealed ultra-smooth surfaces of patterned MAPbBr<sub>3</sub> monocrystalline thin films with these four patterns. The crystal edges of the patterned monocrystalline thin films were given in Figure 2a and b, where clear and sharp edges of nanopatterns were seen. It was clear from the cross-sectional SEM images of Figures 2c and d, that the depth information from the mask was transferred to the perovskite surface pattern successfully. Here, the pattern depth in Si mask was designed to be 600 nm, and the depths of the nanopatterns on monocrystalline thin films were approximately 600 nm with the thin-film thickness at approximately 5 μm and 10 μm for films produced with the patterns shown in Figures 2c and d, respectively. Smaller nanopatterns were also made on MAPbBr<sub>3</sub> thin films using PDMS templates copied from a DVD. Figures 2e and f are the top-view SEM images of a DVD metal surface and the same DVD-surface patterned perovskite monocrystalline thin film, respectively.



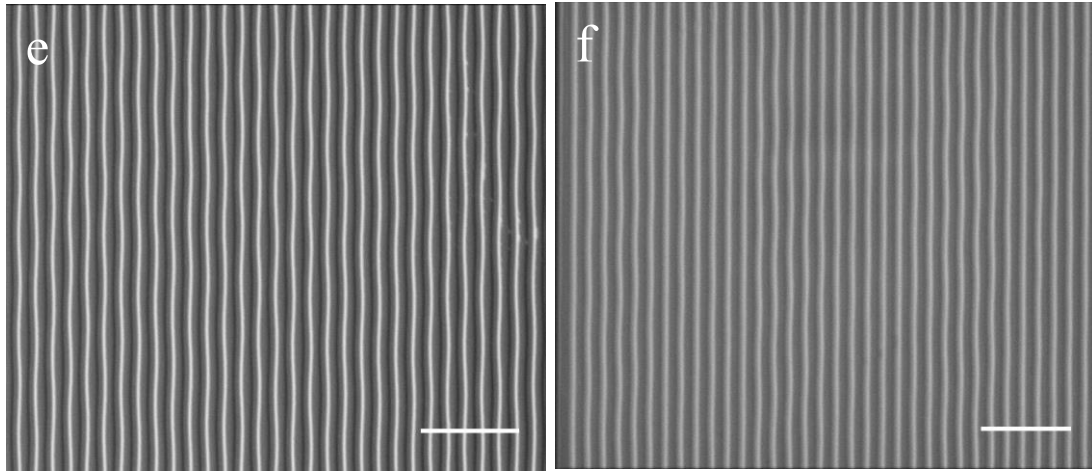


**Figure 2.** SEM images of and MAPbBr<sub>3</sub> monocrystalline thin films with different patterns and a DVD metal surface as a nanopattern template. (a) and (b) Clear and sharp edges of patterns on monocrystalline thin films surfaces. Cross-sectional SEM images of patterned monocrystalline thin films with different thicknesses (c) Pattern 4: 5  $\mu\text{m}$  thickness (d) Pattern 4: 10  $\mu\text{m}$  thickness. (e) DVD metal surface used as the template. (f) Monocrystalline thin film with the same pattern as that on the DVD metal surface in (e). Scale bars: (a-b) 20  $\mu\text{m}$ , (c-f) 5  $\mu\text{m}$ .

Atomic force microscopy (AFM) was conducted on the DVD metal surfaces, PDMS templates and patterned monocrystalline perovskite thin films, by randomly selecting a 10  $\mu\text{m} \times 10 \mu\text{m}$  area. As shown in Supporting Information S5, the DVD had a smooth metal surface with a fine grating structure and a depth of approximately 80 nm. Supporting Information S5d-f were AFM images for the PDMS templates copied directly from the DVD surfaces, revealing a smooth surface and a similar depth to that of the DVD (a few nanometre difference at the bottom might be due to the resolution limit of standard PDMS template made from Sylgard 184<sup>37</sup>). Figures 3a-c were the AFM images of the patterned monocrystalline thin films copied from the PDMS templates, displaying a smooth surface. The results presented in Supporting Information S5 and Figure 3 showed that, by using our epitaxial growth method, nanopatterns were accurately transferred from the template. Additional SEM and AFM images of patterned monocrystalline thin films were provided in Supporting Information S4e and f and S5 to demonstrate the effectiveness of our method.

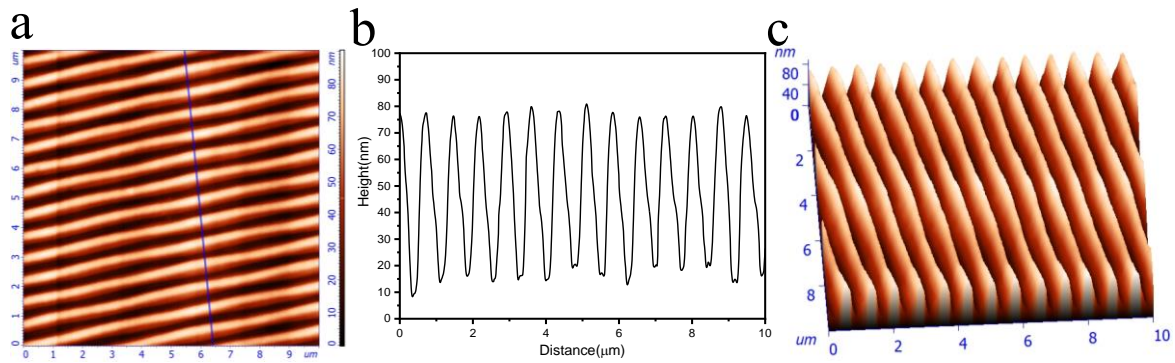


**Figure 3. AFM images of the monocrystalline perovskite surface nanopattern copied from the DVD template:** (a) 2D AFM image; (b) height profile; and (c) 3D AFM image of the nanopatterned single crystal surface.

The crystal structure of the  $\text{MAPbBr}_3$  bulk crystal and nanopatterned monocrystalline thin films were characterised using both single crystal and powder X-ray diffraction methods. As illustrated in Figure 4a, the X-ray powder diffraction patterns of  $\text{MAPbBr}_3$  powder exhibits sharp peaks at  $14.90^\circ$ ,  $21.11^\circ$ ,  $30.07^\circ$ ,  $33.86^\circ$ ,  $37.20^\circ$ ,  $43.05^\circ$ , and  $45.77^\circ$ , corresponding to the (100), (110), (200), (210), (211), (220), and (300) planes. A diffraction pattern taken from the largest crystal face of a  $\text{MAPbBr}_3$  single crystal shows only (100), (200), (300) and (400) diffraction peaks, suggesting predominantly well-structured  $\text{MAPbBr}_3$  single-crystal material. The patterned thick and thin films all exhibit the (100) crystallographic planes. Restricted by the thickness, for the patterned thin film, only (100) and (200) planes are found to match with the Bragg diffraction equation  $2nd = k\lambda$  ( $k = 1, 2, 3, \dots$ ), where  $n$ ,  $d$ , and  $\lambda$  are the refractive index, the thin-film thickness, and light wavelength, respectively. The diffraction data suggest that the  $\text{MAPbBr}_3$  bulk single crystal, nanopatterned films exhibit a cubic crystal structure in space group  $Pm\bar{3}m$ ,<sup>29, 33</sup> with a calculated lattice constant of  $5.93 \text{ \AA}$  at room temperature. The patterned nanostructures exhibit the same crystallography as that of the non-patterned thin film, which implies that the patterned nanostructures are formed by the epitaxial growth of the monocrystalline thin film.

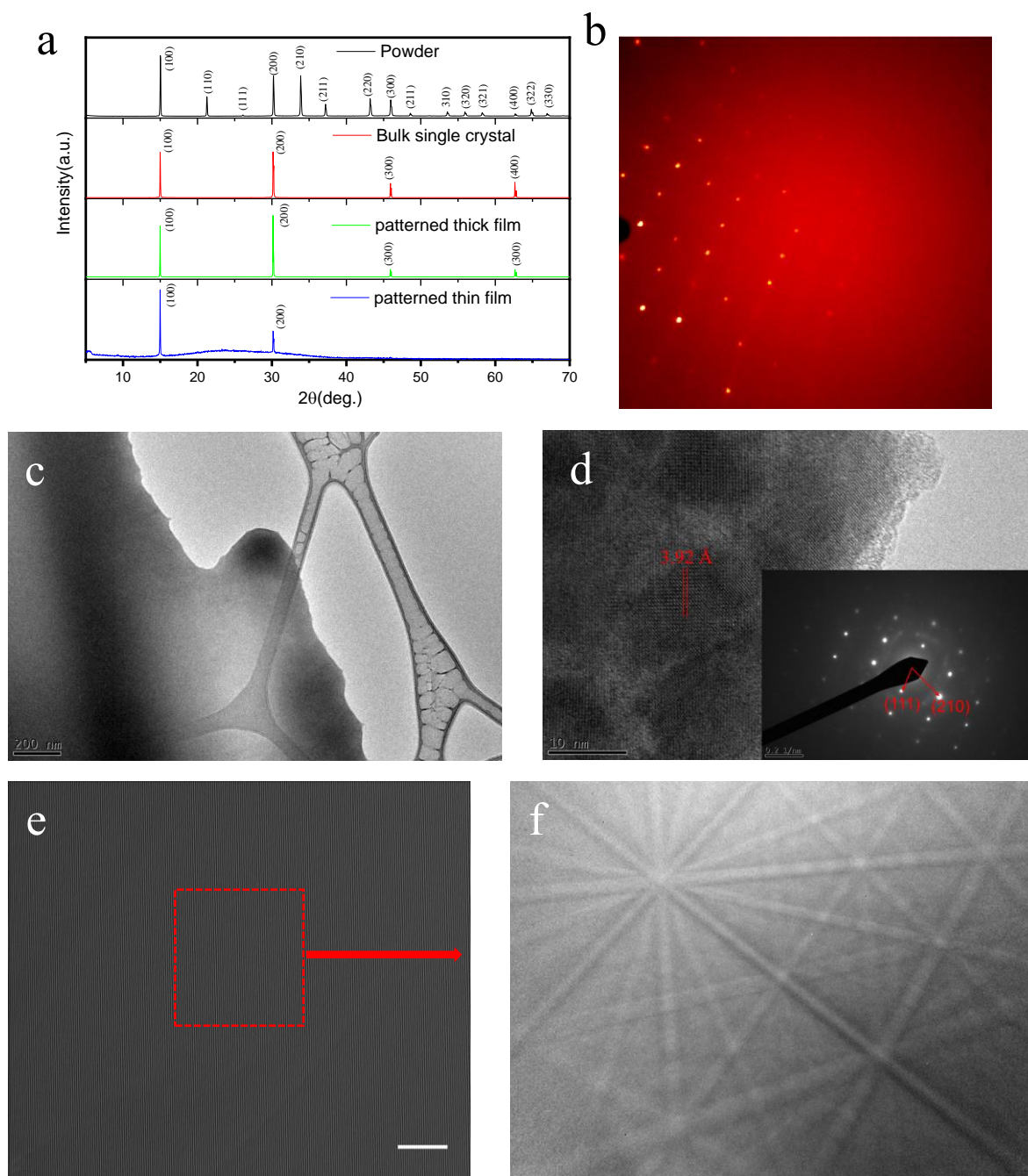


**Figure 4.** (a) X-ray powder diffraction patterns of MAPbBr<sub>3</sub> powder, the largest crystal face of a large MAPbBr<sub>3</sub> bulk single crystal, patterned thick and thin films. (b) Reciprocal lattice image of a single crystal fragment from a perovskite surface patterned thin film prepared by the two-step process using a line-patterned mould consisting of strip 1500 nm and trench 740 nm. (c, d) TEM image, HRTEM image and selected area electron diffraction pattern (inset) of a single-crystal perovskite patterned thin film, with the *d*-spacing measured assigned to the (111) lattice plane. (e) An SEM image of the top view of a monocrystalline thin film with surface nanopatterns. Dashed red rectangular region was selected for EBSD measurement. Scale bar: 20 μm. (f) The corresponding Kikuchi pattern of the selected area from Figure 4e.



To study the single-crystal structure of the surface patterned perovskite thin film, single crystal X-ray diffractometry, transmission electron microscopy (TEM), and electron backscatter diffraction (EBSD) measurements were performed. Figure 4b showed a reciprocal lattice image taken from a surface patterned single crystal fragment of an MAPbBr<sub>3</sub> film where the sharp and strong isolated reflection spots without the presence of powder arcs indicated that the patterned film was single crystal. The structure was confirmed as being cubic in space group  $Pm-3m$  with  $a = 5.9277(9)$  Å at 100 K. Additional 2D-XRD measurements were performed on a nanopatterned single crystal sample (~5 mm in size), and the sharp and strong isolated reflection spots were observed in both 2-theta scan (Supporting Information S6) and chi ( $\chi$ ) scan results (Supporting Information S7). There was no evidence of twinning in the single-crystal data and the heavy atom positions were well resolved and agreed well with published data. In addition, the sample was characterised by TEM (see Figure 4c), where the inset was the corresponding selective area electron diffraction (SAED) pattern image from the red rectangular region marked on the picture, exhibiting only reflections related to the cubic structure with viewing direction along the  $[\bar{1} 2 \bar{1}]$  zone axis. This confirmed the single-crystal nature of the perovskite film. The patterned perovskite film was further investigated using high-resolution (HR) TEM. Figure 4d showed the crystal lattice image with a lattice spacing of 3.92 Å, corresponding to the perovskite (111) plane.

In our EBSD measurements, we noted that the single-crystalline perovskite sample was sensitive to long-time high-energy electron beam irradiation. This was because, when we collected a Kikuchi pattern from a small high-intensity spot, the Kikuchi pattern was firstly seen very clearly for a brief period of time but then faded and disappeared as the sample was melt under the intense current at that high-intensity spot. Therefore, standard EBSD mappings using a high-intensity small spot were not conducted and the striped nanostructure was not studied individually. Instead, we studied a larger area of approximately 50  $\mu\text{m}$  by 50  $\mu\text{m}$  with many striped nanostructures as a whole, by scanning the beam across this area to obtain an average Kikuchi pattern. Figure 4e was an example SEM image of a selected 50  $\mu\text{m}$  by 50  $\mu\text{m}$  area, and Figure 4f was its corresponding Kikuchi pattern, which suggested that the whole nanostructured area was coherent monocrystalline. This was because if there were multiple grains, the Kikuchi map obtained would be composed of multiple overlapping Kikuchi maps or blurred. The effect of the electron beam on this sample for the large area EBSD measurements was investigated too. We noted that there were only some images contrast difference (marked as ellipses) and the Kikuchi

pattern remained unchanged after 30-second 10 kV electron beam irradiation under the scanning approach (Supporting Information S8).

To prove the whole perovskite sample was the same coherent monocrystalline structure, we conducted translation-independent regional mappings of Kikuchi patterns. Firstly, EBSD images were taken on a partially patterned sample. As shown in Figure 5, in a small region, seven different spots from the patterned area, non-patterned area, and the junction revealed identical Kikuchi patterns indicating these regions were in the same crystal orientations. Secondly, EBSD patterns were taken from a relatively large nanopatterned single crystal sample (approximately 5 mm in size) from different locations (Supporting Information S9), where identical crystallographic orientations of the single crystal were also seen clearly.

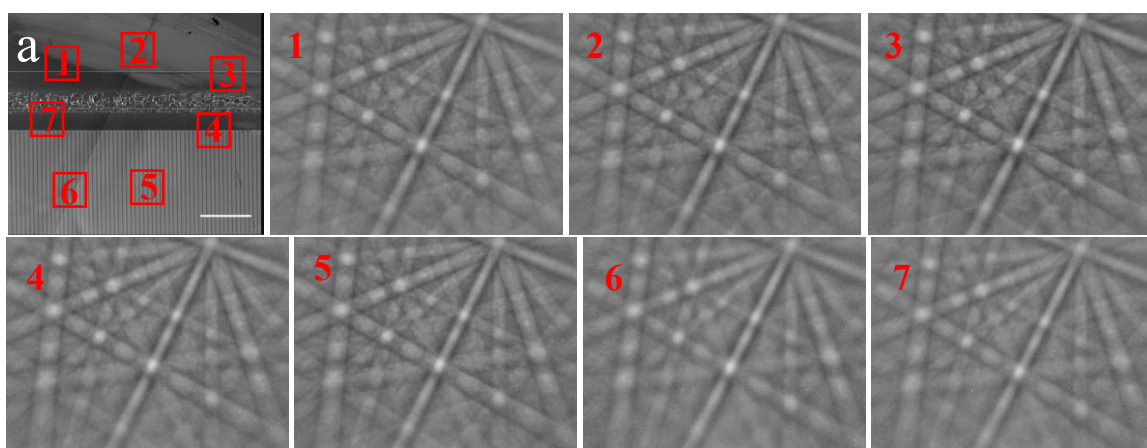


**Figure 5.** (a) A top-view SEM image of a partially patterned MAPbBr<sub>3</sub> plate. (1-7) EBSD data captured from this plate revealing identical Kikuchi patterns at seven different locations corresponding to the marked areas in (a), suggesting that the sample was monocrystalline. Scale bar: 100  $\mu$ m.

The above experimental evidences proved the epitaxial growth of the surface single-crystal patterns using our method. The largest patterned single crystal thin film achieved in our experiment was several millimeters in size, and we believed that the size of the sample film could be further increased with a carefully tailored engineering approach, for example, by continuously supplying fresh sample solutions during the crystal growth and by controlling the experimental conditions such as the temperature and pressure more accurately.<sup>32</sup>

Energy-dispersive X-ray spectroscopy (EDX) element mapping of the patterned monocrystalline thin film was given in Figure 6, confirming the presence of lead (Pb), bromine (Br) and nitrogen (N). The element mapping

spectrum (Supporting Information S10) demonstrated an atomic ratio of 1:3:1, close to the theoretical stoichiometry of Pb, Br and N in  $\text{CH}_3\text{NH}_3\text{PbBr}_3$ .

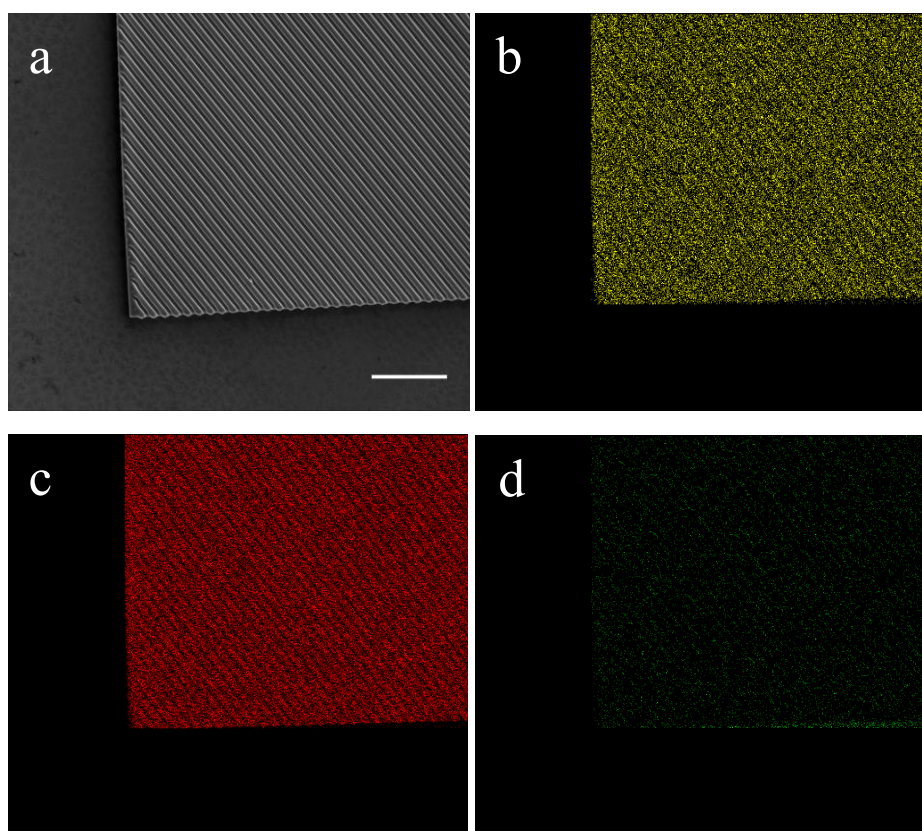
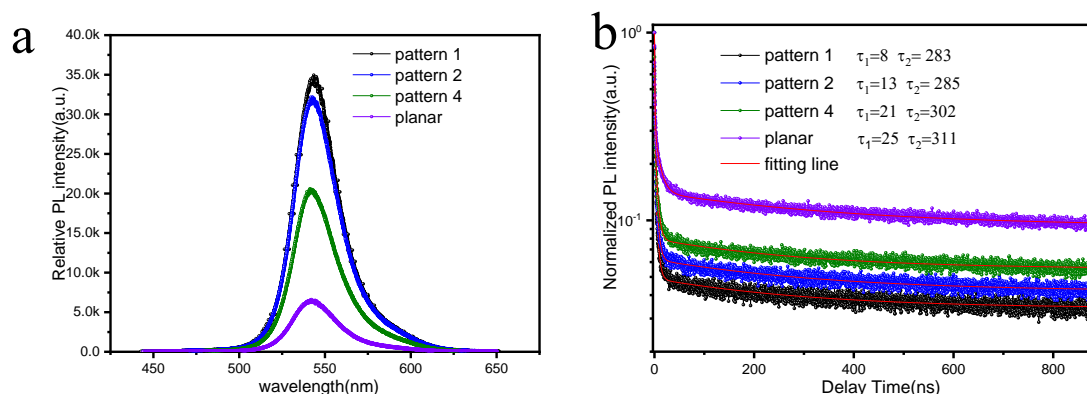


**Figure 6.** (a) Top-view SEM image of patterned  $\text{MAPbBr}_3$  monocrystalline film and corresponding EDX elements mapping images of (b) Pb, (c) Br and (d) N component. Scale bar: 20  $\mu\text{m}$ .

The impressive performance of hybrid perovskite optoelectronics and photovoltaics is attributed to their long carrier lifetimes and high photoluminescence (PL) efficiencies. The PL intensities and lifetimes vary at different grain sizes in the same polycrystalline thin film.<sup>38</sup> Even for single crystals, the surface quality at different areas can affect the PL and decay dynamics.<sup>39</sup> As shown in Figure 7, interesting PL properties of the single-crystal perovskite thin films with nanopatterns are observed in our experiment. Figure 7 a shows the PL emission spectra for nanopatterned perovskite monocrystalline thin films made using our solution-based method under the same experimental conditions. The stripe widths of these patterns range from 600 nm to 3000 nm. A drastic reduction in the PL intensity is seen as the increase of the stripe width (the same trench width). PL intensity from the patterned monocrystalline perovskite thin film Pattern 1 is approximately 2 times higher than that from the patterned monocrystalline perovskite thin film Pattern 4, and is about 7 times higher than the PL intensity from the non-patterned monocrystalline thin film.

Figure 7b shows the time-resolved PL spectra for Pattern 1, Pattern 2, Pattern 4 and flat monocrystalline thin films of the same thickness (10  $\mu\text{m}$ ). Biexponential fitting<sup>39</sup> was conducted to determine the fast ( $\tau_1$ ) and slow ( $\tau_2$ ) dynamics. Our results show that unpatterned monocrystalline thin film has a fast decay lifetime of 25 ns and a slow decay lifetime of 311 ns, in accordance with the reported figures for MAPbBr<sub>3</sub> bulk single crystal.<sup>40</sup> Interestingly, these four Patterns have different surface components ( $\tau_1$ ) but similar bulk components ( $\tau_2$ ). Compared with unpatterned thin films, the fast decay lifetime of Pattern 1 is shortened by a factor of  $\approx 3$ . This suggests that the surface nanopattern influences the behaviour of surface carrier recombination, whilst it has a negligible effect on the carrier diffusion and recombination deep inside the material.

To gain an insight into the origin of the enhanced PL emission with surface nanopatterns, we analysed the thin films under a confocal fluorescence microscope. Confocal fluorescence images and their corresponding reflection images are presented in Figure 7c-f. We found that for both monocrystalline perovskite thin-film patterns, (Pattern 1, 600nm-wide nanostripe and Pattern 4, 3000nm-wide nanostripe), the PL emission mostly occurs on the nanostripe surfaces, while the surface nanotrenches are nearly nonluminous. The PL emission intensity integral curves of confocal fluorescence microphotographs are given in Supporting Information S11, where the patterned thin-film samples with narrower nanostripes display higher PL emission intensity. This agrees with the results in Figure 7a.



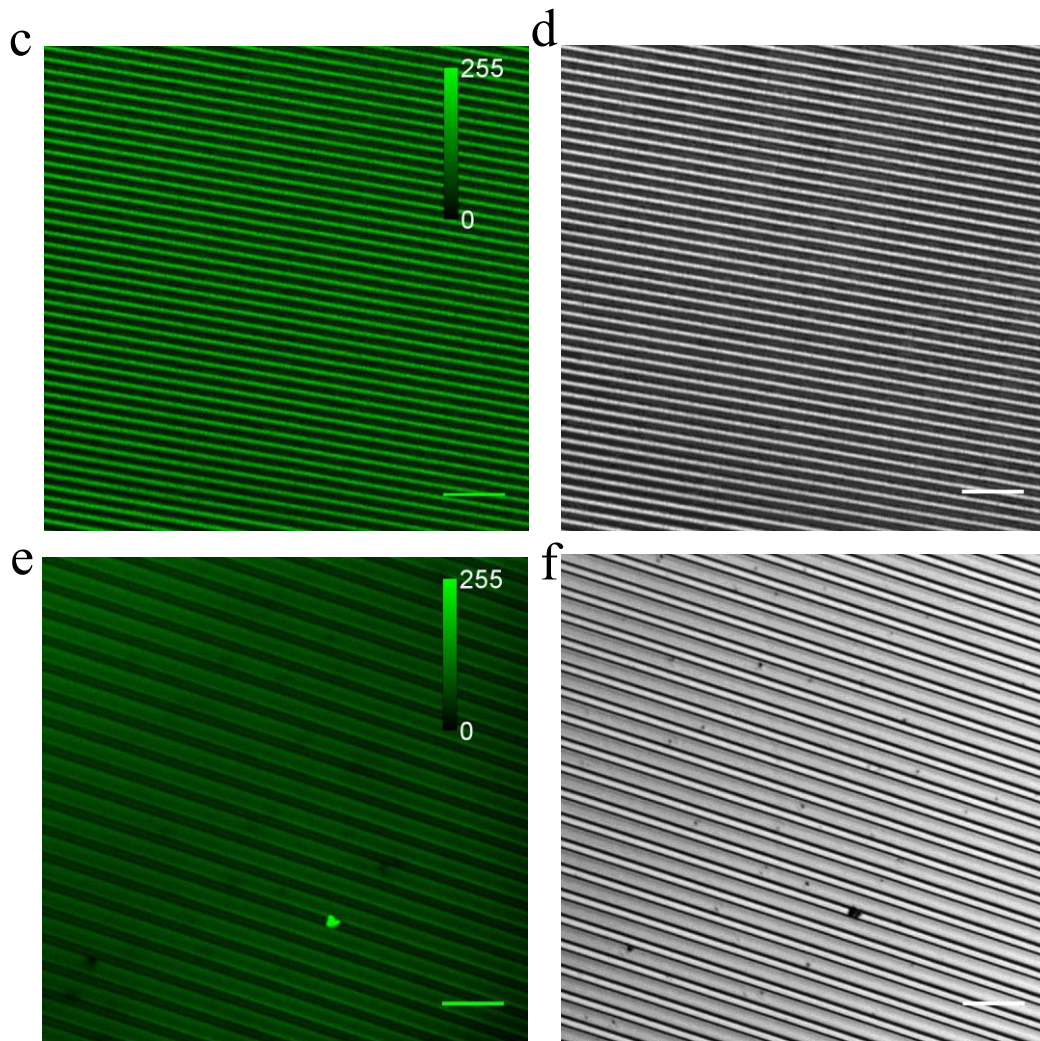


**Figure 7.** Photoluminescence characterizations of samples with different surface pattern parameters. Steady-state PL spectra (a) and Time-resolved PL spectra (b) for Pattern 1, Pattern 4 and flat MAPbBr<sub>3</sub> monocrystalline thin films. Confocal fluorescence microscope images for Pattern 1 (c) and Pattern 4 (e) MAPbBr<sub>3</sub> monocrystalline thin films. And the corresponding optical white light reflective images for Pattern 1(d) and Pattern 4 (f), respectively. Scale bars: 10  $\mu\text{m}$ .

In this section, we attempt to interpret the observed interesting PL phenomenon *via* several possible effects. We attribute the enhanced PL to the combination of two effects, namely increased optical absorption as a result of light coupling<sup>14, 41-44</sup> and Mie resonances induced local-field enhancement on the patterned nanostructure surface.<sup>44, 45</sup>

We first consider the surface nanostructures as subwavelength gratings, which trap photons and enhance their chance of being absorbed. We quantify its effect using rigorous-coupled wave analysis (RCWA).<sup>28</sup> Figure 8a shows the calculated absorption spectra for the perovskite surface nanostructure. The perovskite surface nanostructure Pattern 1 demonstrates the highest absorption (> 86%) and a broadband spectrum for both transverse electric (TE) and transverse magnetic (TM) fields. For comparison, we compute the absorption spectrum for

a planar perovskite in Figure 8a, showing an optical absorption of around 71%. Thus, a 15% enhancement of optical absorption is achieved with the perovskite surface nanostructure of Pattern 1. The photon induced electrons and holes are then recombined radiatively to release photons at a different wavelength (PL wavelength) compared to that of the original excitation photon. Restricted by photolithography conditions in our lab, the smallest grating period fabricated is 2100 nm (Pattern 1).

Mie resonance induced local-field enhancement may be another explanation to the PL enhancement as a result of the surface nanopattern.<sup>46</sup> Figure 8b is the numerical simulation result of the near field at 615 THz (PL excitation frequency, corresponding to a wavelength of 488 nm) for Pattern 1, revealing a resonance electrical field within the nanostructure. A 1.8-fold field enhancement is achieved within the nanostructure, as suggested by our simulation. This resonance field leads to the enhanced radiative recombination of electrons and holes.

According to the analysis above, the observed PL intensity enhancement may be a result of the combination of the increased overall optical absorption caused by the surface subwavelength gratings and Mie resonance induced local electrical-field enhancement in nano-stripes. In addition, as schematically shown in Figures 8c and d, when light strikes the surface of the MAPbBr<sub>3</sub> single crystal, a higher concentration of charge carriers is yielded within the nanostripes. This is because the nanostripe widths 600 nm-3000 nm is smaller than the carrier diffusion length of MAPbBr<sub>3</sub> single crystal<sup>30, 40</sup> and therefore provides a more effective PL region with more radiative charge carriers. This also explains our observation in the confocal microscopy results given in Figure 7c and e, where nanostripes are much brighter compared to nanotrench regions. Furthermore, the PL decay time, especially the fast decay time ( $\tau_1$ ), decreases considerably for nanopatterned thin films in comparison with that for the smooth thin film. This phenomenon may originate from Purcell effect, which suggests that in a resonant cavity, spontaneous emission rate is accelerated by the nanostructure.<sup>45, 47</sup>

The analysis carried out above only aims to provide an approximate explanation to the PL enhancement effect observed in our samples. To understand quantitatively the physics behind the observed PL enhancement, further theoretical analysis must be conducted.

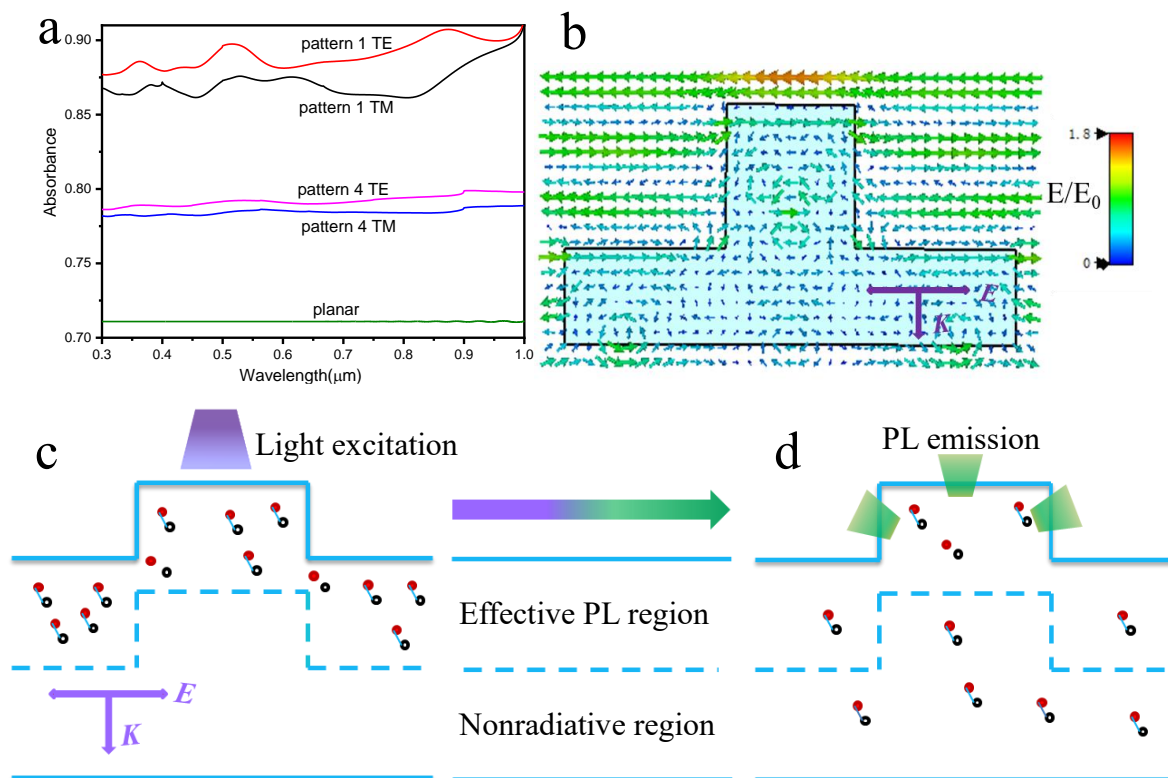


**Figure 8.** Patterned perovskite absorber showing (a) high absorption and a broadband spectrum for both TE- and TM-polarizations. (b) Structure of near-field electric distribution of the grating absorber under normal plane-wave incidence for Pattern 1. Dynamic schematic of charge carrier diffusion and recombination in nanopatterned MAPbBr<sub>3</sub> monocrystalline thin films. (c) Light absorption on the surface and charge carrier generation upon excitation. (d) Charge carriers move inside the crystal and then recombine to release photons to form PL emission.

## CONCLUSIONS

In summary, we demonstrate solution-processed surface-nanopatterning of hybrid perovskite monocrystalline thin films. Based on epitaxial growth in solution, our method ensures top-quality nanopatterns with ultra-smooth surfaces and high material purity. Patterning of arbitrarily shaped micro- and nano-structures has been achieved with accuracy down to a few nanometres. Our method is universal and can be extended to other semiconductor single-crystal nanopatterns. In addition, the demonstrated various PL emission strength and decay times on different surface nanopatterned thin films suggest that carrier properties can be tailored by surface-nanopattern parameters. These results are promising for the realization of nanometre-scale high-performance optoelectronic devices on perovskite single-crystal thin films.

## EXPERIMENTAL

**Chemicals and reagents:** MABr (99%), PbBr<sub>2</sub> ( $\geq 98\%$ ), lead iodide (99%), DMF (anhydrous, 99.8%), trichloro (1H,1H,2H,2H-perfluorooctyl) silane (97%) were purchased from Sigma Aldrich. Dow Corning Sylgard 184 kit was purchased from Ellsworth Adhesives Europe Ltd. All chemicals were used as received without any further purification.

**Preparation of PDMS templates:** A variety of 2 x 2 cm<sup>2</sup> PDMS (polydimethylsiloxane) templates (around 3 mm thick) were fabricated by curing the silicone elastomer and its curing agent (Sylgard 184, Dow Corning) in a 10:1 weight ratio on DVD and pre-patterned Si masters and cutting 2 x 2 cm<sup>2</sup> fully patterned sections out of the elastomer. The Si master used in this work contains line patterns with stripe widths ranging between 600 nm and 3000 nm and a depth of 600 nm. The Si master was cleaned with a CO<sub>2</sub> snowjet, oxygen plasma for 30 minutes and silanized before pouring PDMS over its patterned surface.<sup>48</sup> The DVDs were cut into rectangular-shaped pieces. The protective polycarbonate coating was then removed to expose the metallic surface. The DVD master was rinsed with ethanol and water in order to eliminate dye, dust and polycarbonate remains and finally dried with a flux of nitrogen.<sup>49</sup> To silanize the master, we used a vacuum process inspired by the work of Xia *et. al.*<sup>50</sup> Here, 10  $\mu$ L of trichloro (1H,1H,2H,2H-perfluorooctyl) silane was added to a desiccator containing the Si master, in an argon-filled glove box. Once brought under vacuum, silanization took place overnight and the Si master was stored thereafter. The elastomer was degassed to remove all air bubbles, cured at 80 °C for 1h, and then peeled gently off the master.

**Perovskite Patterned Monocrystalline Thin-Film Preparation:** The perovskite solution was prepared by dissolving a 1:1 molar ratio of PbBr<sub>2</sub> and MABr in DMF solvent mixture in a N<sub>2</sub> glovebox. The resulting concentration was 0.7g/ml.<sup>51</sup> The solution was stirred for 12 h and filtered using PTFE filter with 0.2  $\mu$ m pore size. The solution was then filled into the gap between two substrates and heated at 80 °C for 2-4 h, then the temperature was decreased to 60 °C slowly, the upper substrate was changed into a patterned PDMS or Si master, and repeat the capillary action process, the solution was preheated at 60 °C. After another 2-4 h, the patterned monocrystalline thin films with several millimeters in width were harvested.

**Photoluminescence measurements:** Steady state photoluminescence spectra were collected by using a fluorescence spectrometer (FLS920, Edinburgh



Instruments). The samples were excited using 488 nm light at room temperature. The time-resolved photoluminescence was dispersed in a Triax 550 spectrometer and detected using a Hamamatsu R5509-72 IR-PMT. A picosecond 488 nm pulse laser (Panther OPO ND: YAG) with a pulse width of 5 ns and a repetition rate of 10 Hz was used to excite the perovskite.

**Fluorescence microscopy:** Images were recorded using a confocal microscope (Leica TCS SP2) with a 488 nm laser as the light source.

**Morphological and structural characterization:** The SEM images of MAPbBr<sub>3</sub> monocrystalline thin films were obtained using JEOL JEM7600F, FEI Nova NanoSEM 650, operating in low-vacuum mode with an accelerating voltage of 5 kV. The chemical composition of the thin films was determined by means of EDX (attached to FEI Tecna F20) at voltage of 10 kV. The EBSD analysis was performed at a voltage of 10 kV. All the AFM, experiments were performed in tapping mode under ambient conditions (Dimension ICON SPM system, Bruker, USA). Commercial silicon tips with a nominal spring constant of 40 N m<sup>-1</sup> and resonant frequency of 300 kHz were used in all the experiments. X-ray powder diffraction data were collected using a Bruker D8 Advance diffractometer in Bragg-Brentano geometry and operating with Ni filtered Cu K $\alpha$  radiation ( $\lambda = 1.5418 \text{ \AA}$ ) over the  $2\theta$  range from 5° to 70°. Single crystal X-ray diffraction data were collected using a Bruker Apex II Duo diffractometer using Mo K $\alpha$  radiation (0.7107  $\text{\AA}$ ) at 100 K. Measurements were performed on a small fragment (0.067 mm  $\times$  0.273 mm  $\times$  0.315 mm) cut from a large surface patterned single crystal plate of MAPbBr<sub>3</sub>. A total of 156 frames were collected with a total exposure time of 1.73 h. The frames were integrated with the Bruker SAINT software package using a narrow-frame algorithm.<sup>52</sup> The integration of the data using a cubic unit cell yielded a total of 2148 reflections to a maximum  $\theta$  angle of 45.42° (0.50  $\text{\AA}$  resolution). The final cell constants of  $a = 5.9277(9) \text{ \AA}$ , volume = 208.29(9)  $\text{\AA}^3$ , were based upon the refinement of the XYZ-centroids of 1205 reflections above  $20 \sigma(I)$  with  $6.873^\circ < 2\theta < 90.36^\circ$ . Data were corrected for absorption effects using the multi-scan method (SADABS).<sup>53</sup> The ratio of minimum to maximum apparent transmission was 0.055. The structure was solved by intrinsic phasing using SHELXTL<sup>54</sup> and refinement was carried out using SHELXL.<sup>55</sup> The crystallinity analysis of the patterned thin films was determined *via* a transmission electron microscope (TEM, JEM 2100F, JEOL.) at an accelerating voltage of 200 kV with a camera length of 40 cm. The TEM samples of the surface patterned perovskite plate were firstly scratched from substrate using a razor blade and then made into powder. Further confirmation of the single crystal nature of films was obtained using 2D X-ray diffraction images on a Bruker Apex II Duo diffractometer

using Mo K $\alpha$  radiation (0.7107 Å). Images were collected on a nanopatterned single crystal plate (~5 mm in size) mounted on a glass substrate at selected values of  $\chi$  (with  $\phi$  fixed at 80° and  $2\theta$  at °) and  $2\theta$  (with  $\phi$  fixed at 80° and  $\chi$  at 0°).

## ASSOCIATED CONTENT

### Supporting Information

The Supporting Information is available free of charge on the ACS Publications website.

Bulk single crystal surface patterning process; surface patterns on bulk single crystals; SEM images of one-step patterned polycrystalline thin films; additional SEM images of surface patterned monocrystalline thin films; additional AFM images of surface patterned monocrystalline thin films; 2D-XRD results with different scanning modes; effects of electron-beam irradiation on the crystal structure; large sample EBSD patterns; EDX spectra and quantitative elemental analysis; PL intensity integral curves

## AUTHOR INFORMATION

### Corresponding Author

\*(L.S.) E-mail: [l.su@qmul.ac.uk](mailto:l.su@qmul.ac.uk)

### ORCID<sup>®</sup>

Jinshuai Zhang: 0000-0002-8783-5849

Isaac Abrahams: 0000-0002-8606-6056

Haixue Yan: 0000-0002-4563-1100

Martin M. Knight: 0000-0003-3755-1597

Colin J. Humphreys: 0000-0001-5053-3380

Lei Su: 0000-0002-7894-7881

### Author Contributions

J.Z. and L.S. conceived the idea and designed the experiments. J.Z. performed the experiments with the contribution from Q.G. J.Z., and X.L. conducted PL. C.L. and K.W. prepared the Si master. I.A. performed the single-crystal XRD. J.Z. and L.S. analysed the data. J.Z. and L.S. wrote the paper. H.Y., M.M.K., C.J.H. and L.S. provided guidance throughout the work.

## ACKNOWLEDGMENTS

L.S. gratefully acknowledges the financial support from Engineering and Physical Sciences Research Council (grant number EP/L022559/1 and EP/L022559/2); Royal Society (grant numbers RG130230 and IE161214); H2020 Marie Skłodowska-Curie Actions (790666). J.Z. is supported by a PhD Studentship provided by Queen Mary University of London and China Scholarship Council (CSC). We thank V. Araullo-Petersand and R. Bailey at Nanovision Centre, Queen Mary University of London, for TEM and EBSD assistance.

## AFFILIATIONS

School of Engineering and Materials Science, Queen Mary University of London, UK

## REFERENCES

1. Stranks, S. D.; Eperon, G. E.; Giulia Grancini; Menelaou, C.; Alcocer, M. J. P.; Leijtens, T.; Herz, L. M.; Petrozza, A.; Snaith, H. J. Electron-Hole Diffusion Lengths Exceeding 1 Micrometer in an Organometal Trihalide Perovskite Absorber. *Science* **2013**, *342*, 341-344.
2. Xing, G.; Mathews, N.; Sun, S.; Lim, S. S.; Lam, Y. M.; Grätzel, M.; Mhaisalkar, S.; Sum, T. C. Long-Range Balanced Electron and Hole-Transport Lengths in Organic-Inorganic  $\text{CH}_3\text{NH}_3\text{PbI}_3$ . *Science* **2013**, *342*, 344-347.
3. Dong, Q.; Fang, Y.; Shao, Y.; Mulligan, P.; Qiu, J.; Cao, L.; Huang, J. Electron-Hole Diffusion Lengths  $>175 \mu\text{m}$  in Solution-Grown  $\text{CH}_3\text{NH}_3\text{PbI}_3$  Single Crystals. *Science* **2015**, *347*, 967-969.
4. Jeon, N. J.; Noh, J. H.; Yang, W. S.; Kim, Y. C.; Ryu, S.; Seo, J.; Seok, S. I. Compositional Engineering of Perovskite Materials for High-Performance Solar Cells. *Nature* **2015**, *517*, 476-480.
5. Saidaminov, M. I.; Haque, M. A.; Savoie, M.; Abdelhady, A. L.; Cho, N.; Dursun, I.; Buttner, U.; Alarousu, E.; Wu, T.; Bakr, O. M. Perovskite Photodetectors Operating in Both Narrowband and Broadband Regimes. *Adv. Mater.* **2016**, *28*, 8144-8149.
6. Zhu, H.; Fu, Y.; Meng, F.; Wu, X.; Gong, Z.; Ding, Q.; Gustafsson, M. V.; Trinh, M. T.; Jin, S.; Zhu, X. Y. Lead Halide Perovskite Nanowire Lasers with Low Lasing Thresholds and High Quality Factors. *Nat. Mater.* **2015**, *14*, 636-642.

7. Wang, N.; Cheng, L.; Ge, R.; Zhang, S.; Miao, Y.; Zou, W.; Yi, C.; Sun, Y.; Cao, Y.; Yang, R.; Wei, Y.; Guo, Q.; Ke, Y.; Yu, M.; Jin, Y.; Liu, Y.; Ding, Q.; Di, D.; Yang, L.; Xing, G., *et al.* Perovskite Light-Emitting Diodes Based on Solution-Processed Self-Organized Multiple Quantum Wells. *Nat. Photon.* **2016**, *10*, 699-704.
8. Albisetti, E.; Petti, D.; Pancaldi, M.; Madami, M.; Tacchi, S.; Curtis, J.; King, W. P.; Papp, A.; Csaba, G.; Porod, W.; Vavassori, P.; Riedo, E.; Bertacco, R. Nanopatterning Reconfigurable Magnetic Landscapes *via* Thermally Assisted Scanning Probe Lithography. *Nat. Nanotechnol.* **2016**, *11*, 545-551.
9. Fenwick, O.; Bozec, L.; Credgington, D.; Hammiche, A.; Lazzerini, G. M.; Silberberg, Y. R.; Cacialli, F. Thermochemical Nanopatterning of Organic Semiconductors. *Nat. Nanotechnol.* **2009**, *4*, 664-668.
10. Garcia, R.; Knoll, A. W.; Riedo, E. Advanced Scanning Probe Lithography. *Nat. Nanotechnol.* **2014**, *9*, 577-587.
11. Li, Q.; Peer, A.; Cho, I. H.; Biswas, R.; Kim, J. Replica Molding-Based Nanopatterning of Tribocharge on Elastomer with Application to Electrohydrodynamic Nanolithography. *Nat. Commun.* **2018**, *9*, 974.
12. Priolo, F.; Gregorkiewicz, T.; Galli, M.; Krauss, T. F. Silicon Nanostructures for Photonics and Photovoltaics. *Nat. Nanotechnol.* **2014**, *9*, 19-32.
13. Wang, S.; Liu, Y.; Li, G.; Zhang, J.; Zhang, N.; Xiao, S.; Song, Q. Lead Halide Perovskite Based Microdisk Lasers for On-Chip Integrated Photonic Circuits. *Adv. Opt. Mater.* **2018**, *6*, 1701266.
14. Wang, Y.; Wang, P.; Zhou, X.; Li, C.; Li, H.; Hu, X.; Li, F.; Liu, X.; Li, M.; Song, Y. Diffraction-Grated Perovskite Induced Highly Efficient Solar Cells through Nanophotonic Light Trapping. *Adv. Energy. Mater.* **2018**, *8*, 1702960.
15. Wang, H.; Haroldson, R.; Balachandran, B.; Zakhidov, A.; Sohal, S.; Chan, J. Y.; Zakhidov, A.; Hu, W. Nanoimprinted Perovskite Nanograting Photodetector with Improved Efficiency. *ACS Nano* **2016**, *10*, 10921-10928.
16. Pourdavoud, N.; Wang, S.; Mayer, A.; Hu, T.; Chen, Y.; Marianovich, A.; Kowalsky, W.; Heiderhoff, R.; Scheer, H. C.; Riedl, T. Photonic Nanostructures Patterned by Thermal Nanoimprint Directly into Organo-Metal Halide Perovskites. *Adv. Mater.* **2017**, *29*, 1605003.
17. Saliba, M.; Wood, S. M.; Patel, J. B.; Nayak, P. K.; Huang, J.; Alexander-Webber, J. A.; Wenger, B.; Stranks, S. D.; Horantner, M. T.; Wang, J. T.; Nicholas, R. J.; Herz, L. M.; Johnston, M. B.; Morris, S. M.; Snaith, H. J.; Riede, M. K. Structured Organic-Inorganic Perovskite toward a Distributed Feedback Laser. *Adv. Mater.* **2016**, *28*, 923-929.
18. Kagan, C. R.; Breen, T. L.; Kosbar, L. L. Patterning Organic-Inorganic Thin-Film Transistors Using Microcontact Printed Templates. *Appl. Phys. Lett.* **2001**, *79*, 3536-3538.

19. Gu, L.; Tavakoli, M. M.; Zhang, D.; Zhang, Q.; Waleed, A.; Xiao, Y.; Tsui, K. H.; Lin, Y.; Liao, L.; Wang, J.; Fan, Z. 3D Arrays of 1024-Pixel Image Sensors Based on Lead Halide Perovskite Nanowires. *Adv. Mater.* **2016**, *28*, 9713-9721.
20. Mao, J.; Sha, W. E. I.; Zhang, H.; Ren, X.; Zhuang, J.; Roy, V. A. L.; Wong, K. S.; Choy, W. C. H. Novel Direct Nanopatterning Approach to Fabricate Periodically Nanostructured Perovskite for Optoelectronic Applications. *Adv. Funct. Mater.* **2017**, *27*, 1606525.
21. Lee, L.; Baek, J.; Park, K. S.; Lee, Y. E.; Shrestha, N. K.; Sung, M. M. Wafer-Scale Single-Crystal Perovskite Patterned Thin Films Based on Geometrically-Confined Lateral Crystal Growth. *Nat. Commun.* **2017**, *8*, 15882.
22. Liu, P.; He, X.; Ren, J.; Liao, Q.; Yao, J.; Fu, H. Organic-Inorganic Hybrid Perovskite Nanowire Laser Arrays. *ACS Nano* **2017**, *11*, 5766-5773.
23. Liu, X.; Niu, L.; Wu, C.; Cong, C.; Wang, H.; Zeng, Q.; He, H.; Fu, Q.; Fu, W.; Yu, T.; Jin, C.; Liu, Z.; Sum, T. C. Periodic Organic-Inorganic Halide Perovskite Microplatelet Arrays on Silicon Substrates for Room-Temperature Lasing. *Adv. Sci.* **2016**, *3*, 1600137.
24. Wang, G.; Dehui Li; Hung-Chieh Cheng; Yongjia Li; Chih-Yen Chen; Anxiang Yin; Zipeng Zhao; Zhaoyang Lin; Hao Wu; Qiyuan He; Mengning Ding; Yuan Liu; Yu Huang; Duan, X. Wafer-Scale Growth of Large Arrays of Perovskite Microplate Crystals for Functional Electronics and Optoelectronics. *Sci. Adv.* **2015**, *1*, 1500613.
25. Conings, B.; Drijkoningen, J.; Gauquelin, N.; Babayigit, A.; D'Haen, J.; D'Olieslaeger, L.; Ethirajan, A.; Verbeeck, J.; Manca, J.; Mosconi, E.; Angelis, F. D.; Boyen, H.-G. Intrinsic Thermal Instability of Methylammonium Lead Trihalide Perovskite. *Adv. Energy. Mater.* **2015**, *5*, 1500477.
26. Leijtens, T.; Eperon, G. E.; Noel, N. K.; Habisreutinger, S. N.; Petrozza, A.; Snaith, H. J. Stability of Metal Halide Perovskite Solar Cells. *Adv. Energy. Mater.* **2015**, *5*.
27. Xiao, C.; Li, Z.; Guthrey, H.; Moseley, J.; Yang, Y.; Wozny, S.; Moutinho, H.; To, B.; Berry, J. J.; Gorman, B.; Yan, Y.; Zhu, K.; Al-Jassim, M. Mechanisms of Electron-Beam-Induced Damage in Perovskite Thin Films Revealed by Cathodoluminescence Spectroscopy. *J. Phys. Chem. C* **2015**, *119*, 26904-26911.
28. Alias, M. S.; Yang, Y.; Ng, T. K.; Dursun, I.; Shi, D.; Saidaminov, M. I.; Priante, D.; Bakr, O. M.; Ooi, B. S. Enhanced Etching, Surface Damage Recovery, and Submicron Patterning of Hybrid Perovskites Using a Chemically Gas-Assisted Focused-Ion Beam for Subwavelength Grating Photonic Applications. *J. Phys. Chem. Lett.* **2016**, *7*, 137-142.
29. Lei, Y.; Chen, Y.; Gu, Y.; Wang, C.; Huang, Z.; Qian, H.; Nie, J.; Hollett, G.; Choi, W.; Yu, Y.; Kim, N.; Wang, C.; Zhang, T.; Hu, H.; Zhang, Y.; Li, X.; Li, Y.; Shi, W.; Liu, Z.; Sailor, M. J., *et al.* Controlled Homoepitaxial Growth of Hybrid Perovskites. *Adv. Mater.* **2018**, *30*, 1705992.

30. Saidaminov, M. I.; Abdelhady, A. L.; Murali, B.; Alarousu, E.; Burlakov, V. M.; Peng, W.; Dursun, I.; Wang, L.; He, Y.; Maculan, G.; Goriely, A.; Wu, T.; Mohammed, O. F.; Bakr, O. M. High-Quality Bulk Hybrid Perovskite Single Crystals within Minutes by Inverse Temperature Crystallization. *Nat. Commun.* **2015**, *6*, 7586.
31. Saidaminov, M. I.; Abdelhady, A. L.; Maculan, G.; Bakr, O. M. Retrograde Solubility of Formamidinium and Methylammonium Lead Halide Perovskites Enabling Rapid Single Crystal Growth. *Chem. Commun.* **2015**, *51*, 17658-17661.
32. Liu, Y.; Zhang, Y.; Yang, Z.; Yang, D.; Ren, X.; Pang, L.; Liu, S. F. Thinness- and Shape-Controlled Growth for Ultrathin Single-Crystalline Perovskite Wafers for Mass Production of Superior Photoelectronic Devices. *Adv. Mater.* **2016**, *28*, 9204-9209.
33. Chen, Y. X.; Ge, Q. Q.; Shi, Y.; Liu, J.; Xue, D. J.; Ma, J. Y.; Ding, J.; Yan, H. J.; Hu, J. S.; Wan, L. J. General Space-Confined On-Substrate Fabrication of Thickness-Adjustable Hybrid Perovskite Single-Crystalline Thin Films. *J. Am. Chem. Soc.* **2016**, *138*, 16196-16199.
34. Li, Y.; Han, L.; Liu, Q.; Wang, W.; Chen, Y.; Lyu, M.; Li, X.; Sun, H.; Wang, H.; Wang, S.; Li, Y. Confined-Solution Process for High-Quality  $\text{CH}_3\text{NH}_3\text{PbBr}_3$  Single Crystals with Controllable Morphologies. *Nano. Res.* **2018**, *11*, 3306-3312.
35. Rao, H. S.; Chen, B. X.; Wang, X. D.; Kuang, D. B.; Su, C. Y. A Micron-Scale Lamellar  $\text{MAPbBr}_3$  Single Crystal for an Efficient and Stable Perovskite Solar Cell. *Chem. Commun.* **2017**, *53*, 5163-5166.
36. Gao, H.; Feng, J.; Pi, Y.; Zhou, Z.; Zhang, B.; Wu, Y.; Wang, X.; Jiang, X.; Jiang, L. Bandgap Engineering of Single-Crystalline Perovskite Arrays for High-Performance Photodetectors. *Adv. Funct. Mater.* **2018**, *28*, 1804349.
37. Schmid, H.; Michel, B. Siloxane Polymers for High-Resolution, High-Accuracy Soft Lithography. *Macromolecules* **2000**, *33*, 3042-3049.
38. deQuilettes, D. W.; Vorpahl, S. M.; Stranks, S. D.; Nagaoka, H.; Eperon, G. E.; Ziffer, M. E.; Snaith, H. J.; Genge, D. S. Impact of Microstructure on Local Carrier Lifetime in Perovskite Solar Cells. *Science* **2015**, *348*, 683-686.
39. Ding, J.; Lian, Z.; Li, Y.; Wang, S.; Yan, Q. The Role of Surface Defects in Photoluminescence and Decay Dynamics of High-Quality Perovskite  $\text{MAPbI}_3$  Single Crystals. *J. Phys. Chem. Lett.* **2018**, *9*, 4221-4226.
40. Shi, D.; Adinolfi, V.; Comin, R.; Yuan, M.; Alarousu, E.; Buin, A.; Chen, Y.; Hoogland, S.; Rothenberger, A.; Katsiev, K.; Losovyj, Y.; Zhang, X.; Dowben, P. A.; Mohammed, O. F.; Sargent, E. H.; Bakr, O. M. Low Trap-State Density and Long Carrier Diffusion in Organolead Trihalide Perovskite Single Crystals. *Science* **2015**, *347*, 519-522.

41. Konstantatos, G.; Sargent, E. H. Nanostructured Materials for Photon Detection. *Nat. Nanotechnol.* **2010**, *5*, 391-400.
42. Zhu, J.; Yu, Z.; Burkhard, G. F.; Hsu, C.-M.; Connor, S. T.; Xu, Y.; Wang, Q.; McGehee, M.; Fan, S.; Cui, Y. Optical Absorption Enhancement in Amorphous Silicon Nanowire and Nanocone Arrays. *Nano Lett.* **2009**, *9*, 279-282.
43. Ferry, V. E.; Sweatlock, L. A.; Pacifici, D.; Atwater, H. A. Plasmonic Nanostructure Design for Efficient Light Coupling into Solar Cells. *Nano Lett.* **2008**, *8*, 4391-4397.
44. Wang, H.; Liu, S. C.; Balachandran, B.; Moon, J.; Haroldson, R.; Li, Z.; Ishteev, A.; Gu, Q.; Zhou, W.; Zakhidov, A.; Hu, W. Nanoimprinted Perovskite Metasurface for Enhanced Photoluminescence. *Opt. Express* **2017**, *25*, A1162-A1171.
45. Makarov, S. V.; Milichko, V.; Ushakova, E. V.; Omelyanovich, M.; Cerdan Pasaran, A.; Haroldson, R.; Balachandran, B.; Wang, H.; Hu, W.; Kivshar, Y. S.; Zakhidov, A. A. Multifold Emission Enhancement in Nanoimprinted Hybrid Perovskite Metasurfaces. *ACS Photonics* **2017**, *4*, 728-735.
46. Makarov, S. V.; Milichko, V.; Ushakova, E. V.; Omelyanovich, M.; Cerdan Pasaran, A.; Haroldson, R.; Balachandran, B.; Wang, H.; Hu, W.; Kivshar, Y. S.; Zakhidov, A. A. Multifold Emission Enhancement in Nanoimprinted Hybrid Perovskite Metasurfaces. *ACS Photonics* **2017**, *4*, 728-735.
47. Wu, Z.; Chen, J.; Mi, Y.; Sui, X.; Zhang, S.; Du, W.; Wang, R.; Shi, J.; Wu, X.; Qiu, X.; Qin, Z.; Zhang, Q.; Liu, X. All-Inorganic CsPbBr<sub>3</sub> Nanowire Based Plasmonic Lasers. *Adv. Opt. Mater.* **2018**, *6*, 1800674.
48. Harkema, S.; Schäffer, E.; Morariu, M. D.; Steiner, U. Pattern Replication by Confined Dewetting. *Langmuir* **2003**, *19*, 9714-9718.
49. Zanatta, M.; Calvillo, L.; Zheng, J.; Rizzi, G. A.; Durante, C.; Giallongo, G.; Chirkov, D.; Colazzo, L.; Marega, C.; Gennaro, A.; Granozzi, G. Cu<sub>2</sub>O/TiO<sub>2</sub> Heterostructures on a DVD as Easy&Cheap Photoelectrochemical Sensors. *Thin Solid Films* **2016**, *603*, 193-201.
50. Xia, Y.; Whitesides, G. M. Soft Lithography. *Annu. Rev. Mater. Sci.* **1998**, *28*, 153-184.
51. Liu, Y.; Zhang, Y.; Yang, Z.; Feng, J.; Xu, Z.; Li, Q.; Hu, M.; Ye, H.; Zhang, X.; Liu, M.; Zhao, K.; Liu, S. Low-Temperature-Gradient Crystallization for Multi-Inch High-Quality Perovskite Single Crystals for Record Performance Photodetectors. *Mater. Today* **2019**, *22*, 67-75.
52. Bruker. *SAINT - Data Reduction Software*, Version 2015/9; Bruker AXS Inc.: Madison, WI, USA, 2015.
53. Bruker. *SADABS - Area Detector Scaling and Absorption Correction*, Version 2014/5; Bruker AXS Inc.: Madison, WI, USA, 2014.

54. Sheldrick, G. M. SHELXT-Integrated Space-Group and Crystal-Structure Determination. *Acta Crystallogr., Sect. A: Found. Adv.* **2015**, *71*, 3-8.
55. Sheldrick, G. M. Crystal Structure Refinement with SHELXL. *Acta Crystallogr., Sect. C: Struct. Chem.* **2015**, *71*, 3-8.